Shelf Cross-Shore Flows under Storm-Driven Conditions: Role of Stratification, Shoreline Orientation, and Bathymetry

XIAODONG WU AND GEORGE VOULGARIS

School of the Earth, Ocean and Environment, University of South Carolina, Columbia, South Carolina

NIRNIMESH KUMAR

Department of Civil and Environmental Engineering, University of Washington, Seattle, Washington

(Manuscript received 1 May 2017, in final form 26 June 2018)

ABSTRACT

Numerical simulations are used to study the response of Long Bay, South Carolina, a typical coastal embayment with curved coastline located on the South Atlantic Bight, to realistic, climatologically defined, synoptic storm forcing. Synoptic storms, consisting of cold and warm fronts as well as tropical storms, are used as forcing under both mixed and stratified initial conditions. The analysis focuses on the development of cross-shore shelf circulation and the relative contributions of regionally defined cross-shore winds and alongshore bathymetric variation. The simulation results show that, under stratified conditions, the regionally defined offshore-directed wind component promotes upwelling during the developing stage of the cold front and enhances mixing during the decaying stage. No significant effect is found for warm front and tropical storm forcing conditions. Net cross-shore transports are induced at the southern and northern sides of the embayment that have opposing signs. Besides the surface and bottom Ekman transports, geostrophic transport due to alongshore shelf bed slope and horizontal advection are found to be important contributors to cross-shore flow development. Sea level variability along the curved coastline is driven by the regional alongshore wind, but a spatial variability is identified from the locally defined components of along- and cross-shore winds controlled by coastline orientation.

1. Introduction

The dynamic region extending from the surf zone to the outer shelf is the conduit between the coastline and the open ocean. Material exchange (e.g., pollutants, larvae, and biota) within this region is controlled by cross-shore flows driven by winds, waves, tides, and buoyancy. In the mid- to outer shelf, alongshore wind forcing contributes to the development of a surface and a bottom Ekman layer (e.g., Lentz and Fewings 2012; Brink 2016) that are separated by a distinct intermediate layer (Lentz 2008). In the inner shelf, the surface and bottom boundary layers overlap, and the alongshore wind-driven Ekman transport decreases toward the shoreline (Mitchum and Clarke 1986; Lentz and Fewings 2012).

Cross-shore shelf flows can also develop in response to cross-shore winds (e.g., Tilburg 2003; Fewings et al. 2008; Horwitz and Lentz 2014; Horwitz and Lentz 2016), although with a magnitude smaller than that attributed to alongshore wind forcing. In such a case, a two-layer cross-shore circulation develops with a wind-following flow in the upper water column and a compensating return flow near the seabed (e.g., Fewings et al. 2008). Surface waves, when present, can either enhance or reduce vertical shear in cross-shore flow depending on the cross-shore wind direction (Fewings et al. 2008).

Under stratified shelf conditions, a reduction in vertical transfer of momentum leads to a thinner Ekman layer, limiting the horizontal extent of the inner shelf (e.g., Lentz 2001; Austin and Lentz 2002). In the presence of a horizontal density gradient (higher offshore density), offshore-directed winds can enhance vertical stratification and thus increase cross-shore circulation within the inner shelf. In contrast, shoreward-directed winds enhance vertical mixing and tend to reduce cross-shore circulation (Horwitz and Lentz 2014). Under downwelling-favorable winds, downwelling of surface, light water contributes to vertical mixing. In this case, the cross-shore wind component, if present, controls the transport within the mixed inner shelf. In contrast, under

Corresponding author: Xiaodong Wu, xwu@email.sc.edu

DOI: 10.1175/JPO-D-17-0090.1

© 2018 American Meteorological Society. For information regarding reuse of this content and general copyright information, consult the AMS Copyright Policy (www.ametsoc.org/PUBSReuseLicenses).

Brought to you by NOAA Central Library | Unauthenticated | Downloaded 01/16/24 05:03 PM UTC

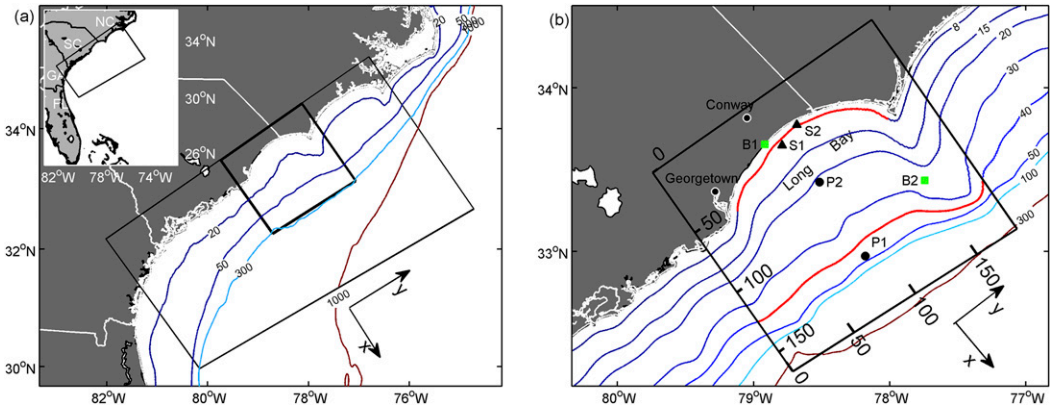

FIG. 1. (a) The study site and the model grid outlines. (b) Close-up of the inner domain (Long Bay) and bathymetry. The green squares show the NOAA/NOS meteorological stations (B1: Springmaid Pier; B2: Frying Pan Shoaling buoy), and the black triangles (sites S1 and S2) are the locations where the data used in model verification were collected. The black dots (sites P1 and P2) are chosen for the current dynamics analysis (see text for details).

upwelling-favorable winds, the inner shelf can become stratified and both the along- and cross-shore wind components contribute to the development of cross-shore circulation (Horwitz and Lentz 2016).

The wind forcing relevant to shelf circulation broadly falls within both the meso- and synoptic scales of meteorological phenomena. Sea breeze, for example, a mesoscale, diurnal event, can enhance shelf circulation in latitudes with a near-diurnal inertial period and under stratified conditions (e.g., Zhang et al. 2009). It can also contribute to the development of upwelling events (e.g., Walter et al. 2017). Synoptic-scale meteorological events have horizontal scales of 1000–6000 km, and they have been categorized into frontal systems (cold and warm fronts) and tropical storms (Mather et al. 1964; Dirks et al. 1988; Muller and Stone 2001; Keim et al. 2004). Although frontal events are less energetic than tropical storms, they occur more frequently and are usually associated with unsteady, rotatory wind velocities (Wu et al. 2017). Previous studies have focused on the broad impacts of these storms on the coastline, especially on their role in developing damaging waves (e.g., Davis and Dolan 1993; Fan et al. 2005), and shelf flows (Austin and Lentz 1999; Gutierrez et al. 2006; among others).

Multiple studies have contributed to our understanding of shelf circulation, yet most of them have focused primarily on steady/quasi-steady wind conditions and have assumed a relatively straight coastline with alongshore-uniform bathymetry. Earlier studies (e.g., Crépon et al. 1984; Whitney and Allen 2009; Kumar et al. 2013) have shown that changes in coastline orientation can introduce alongshore variability in the relative magnitudes of local along- and cross-shore wind components. Additionally, changes in shelf width or other bathymetric perturbations (i.e., isobath convergence/divergence) can induce alongshore flow veering and the development of cross-shore currents (Arthur 1965). Typical examples are upwelling enhancement downstream of capes (Blanton et al. 1981; Gan and Allen 2002) or before the flows encounter an increase in shelf width (Pringle 2002).

In this study, we examine shelf circulation dynamics focusing on cross-shore flows, under nonsteady wind forcing conditions associated with realistic storm events. The study is conducted in Long Bay (see Fig. 1), a coastal embayment with a curved coastline located in the South Atlantic Bight (SAB), which frequently experiences cyclogenesis (Bradbury et al. 2003). Our goal is to examine cross-shore flow development and the relative contributions of the along- and cross-shore components of wind forcing and that of bathymetric effects. Numerical simulations of shelf circulation, forced with winds associated with types of storms that dominate the wind forcing in this location, are utilized for this analysis. The results are used to examine the alongshore variation of the cross-shore transport within the embayment and to reveal the underlying mechanisms. The numerical model configuration, verification, and utilization are presented in section 2, while section 3 describes the shelf circulation patterns induced by the variable wind forcing under both mixed and stratified shelf conditions. Flow dynamics as revealed through the modeling and momentum balance analysis are discussed in section 4. Finally, a summary and conclusions are given in section 5.

2. Methodology

a. Model configuration

Shelf circulation is simulated using the Regional Ocean Modeling System (ROMS) under the framework

Brought to you by NOAA Central Library | Unauthenticated | Downloaded 01/16/24 05:03 PM UTC

of the Coupled Ocean–Atmosphere–Wave–Sediment–Transport (COAWST) modeling system (Warner et al. 2010; Kumar et al. 2012). ROMS is a three-dimensional, free-surface, hydrostatic numerical model that has a stretched terrain-following vertical coordinate (Shchepetkin and McWilliams 2005). In the present implementation, a domain much larger than the area of interest (see Fig. 1) is used to avoid boundary effects. This domain extends over a large portion of the SAB (see Fig. 1a), covering an area of 301 km × 597 km with horizontal resolutions of 720 and 830 m in the cross-shore x and alongshore y directions, respectively. Hereinafter, cross-shore is defined as in the x direction, unless otherwise specified. The stretched vertical domain consists of 30 sigma levels. Closure of the vertical mixing of momentum and tracer is achieved via a k–ε turbulence closure scheme (Umlauf and Burchard 2003). Barotropic (depth independent) velocity and sea level boundary conditions are defined using a combination of Chapman and Flather radiation conditions (Marchesiello et al. 2001), while the standard Orlanski radiation boundary condition (Raymond and Kuo 1984) is used for the depth-dependent flow. Bottom friction is calculated using a linear bottom drag scheme, with a drag coefficient $r_0 = 3 \times 10^{-4}\,\mathrm{m\,s^{-1}}$. The latter was determined during the model verification process described in section 2b.

Surface stress is estimated from the formulation of Large and Pond (1981) using wind velocity time series. The wind velocity vector $\mathbf{U}_w$ was recorded at two sites [NOAA/National Ocean Service (NOS) Springmaid Pier, South Carolina, station 8661070 and NOAA/NDBC Frying Pan Shoaling buoy, station 41013] located on the coastline and some 50 km offshore, respectively (see stations B1 and B2 in Fig. 1b). A comparison of the two wind records (Wu et al. 2017) revealed that offshore wind speeds are consistently higher than those recorded on the coastline. In addition, there is a phase difference between the two locations, exhibited as a variation in wind direction. Here, an empirically derived cross-shore weighed interpolation is used to resolve the cross-shore variable wind velocity vector:

$$\mathbf{U}_w(x) = \begin{cases} (1-x)^8\mathbf{U}_{\mathrm{B1}} + \left[1-(1-x)^8\right]\mathbf{U}_{\mathrm{B2}}, & \text{if} \quad x<1 \\ \mathbf{U}_{\mathrm{B2}}, & \text{if} \quad x \geq 1 \end{cases}, \tag{2.1}$$

where $\mathbf{U}_w$ is the wind velocity vector at normalized cross-shore distance x (with 0 and 1 corresponding to the onshore and offshore boundaries of the area of interest, respectively; see Fig. 1b). The $\mathbf{U}_{\mathrm{B1}}$ and $\mathbf{U}_{\mathrm{B2}}$ are the wind velocity vectors recorded at stations B1 (onshore) and B2 (offshore), respectively. Equation (2.1) provides an accurate representation of the observed rapid weakening of wind velocity close to the coastline (Wu et al. 2017). Its application provides a change in wind speed toward the shoreline resembling that of an exponential decay found in boundary layer flows, indicating the role of the coastline as a lateral boundary for the wind field (Smith and MacPherson 1987).

b. Model verification

Prior to its application, the model was verified by comparing its results with in situ current measurements obtained at two nearshore sites (S1 and S2; see Fig. 1b) during a 28-day period (1–28 February 2004). The corresponding wind velocities for that period are shown in Fig. 2a. Tidal forcing along the open boundaries is prescribed analytically using the tidal constituent values interpolated from the ADCIRC tidal database (Mukai et al. 2002). Water temperature and salinity are kept constant and invariable at the open boundaries during this 28-day period. The simulations were initialized at rest, with the wind and tidal forcing being ramped up over a period of 24 h.

The simulated horizontal currents and sea surface level are compared with the measured values at sites S1 and S2, at water depths of 10 and 9 m, respectively (see Fig. 1b). The subtidal component of both the simulated and measured quantities was estimated using a low-pass filter with a cut-off period of 33 h. The higher-frequency (hereafter referred to as tidal) component was estimated by removing the subtidal signal from the total signal. As the emphasis is on wind-driven currents, the subtidal flow variability, at $z = -1.2$ and $z = -4.2$ m below the sea surface, and the sea level for both the measured and simulated data are shown in Fig. 2. The subtidal circulation patterns at S2 are similar to those at S1 and therefore are not shown here. The corresponding root-mean-square (rms) errors and correlation coefficients r, including those for the tidal components, are listed in Table 1. Here, cross-shore is defined as the direction normal to the local bathymetric contour, with the scale defined over a distance of 4 times the alongshore grid size (i.e., 3.2 km). This scale was chosen as it provides the minimum number of grid cells required to define a general local contour direction; however, the direction did not change when larger length scales (up to 10 grid cells) were used. During the verification period, the area experienced several storm events, including two cold front (CF), one warm front (WF), and one tropical storm (TS) event (see Fig. 2a). At both sites, the simulated tidal components are well correlated with the estimates from the measurements ($r \approx 0.8$). The subtidal sea level fluctuations are less than 0.4 m at this site (Fig. 2b), and the simulated and observed sea levels agree well for the first CF and WF events. During the periods of the

Brought to you by NOAA Central Library | Unauthenticated | Downloaded 01/16/24 05:03 PM UTC

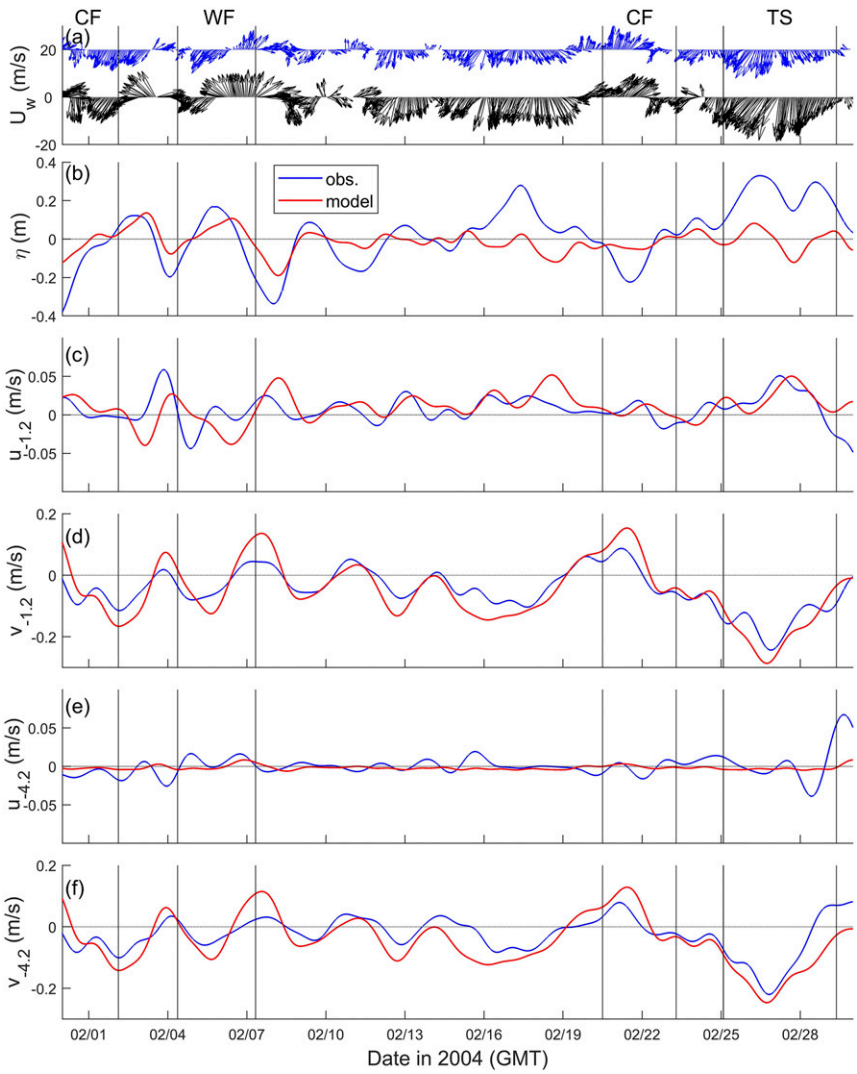

FIG. 2. Comparison of subtidal signal from model (red lines) results and in situ (blue lines) measurements. (a) Wind velocity vectors used for forcing as recorded at the stations B1 (blue) and B2 (black). (b) Sea surface elevation η, (c) cross-shore and (d) alongshore velocity at -1.2 m below the surface, and (e) cross-shore and (f) alongshore velocity at -4.2 m below the surface. Vertical lines delineate the periods of individual storm event.

second CF and the TS events, the sea level is underestimated (<0.2 m) by the model, although its temporal variability is captured well. The subtidal alongshore component of the flow shows a higher correlation than the cross-shore flow component (Figs. 2c–f and Table 1). For site S1, the correlation coefficients of simulated and measured cross-shore velocities, at 1.2 and 4.2 m below sea surface, were increased significantly by rotating the instrument coordinate system by few degrees (a counterclockwise rotation by 8° provides the maximum correlation coefficient), while the correlation coefficients of alongshore velocities showed negligible change. Such a result is not surprising as cross-shore flows are much smaller in magnitude ($<4\,\mathrm{cm\,s^{-1}}$) and measurements of such small currents are easily affected by local bathymetric irregularities and/or small errors in the instrument's compass record.

Overall, we consider the agreement between the simulated and measured values of each parameter satisfactory to allow use of the model to diagnose flow dynamics over the domain.

c. *Modeling storm-induced circulation*

Following verification, the model was used to simulate shelf circulations in response to climatologically defined storms (Wu et al. 2017). The wind vector temporal

Brought to you by NOAA Central Library | Unauthenticated | Downloaded 01/16/24 05:03 PM UTC

TABLE 1. The rms errors and correlation coefficient r of tidal and subtidal sea surface elevation and cross-shore u and alongshore v velocity components at sites S1 and S2 and at elevations −1.2 and −1.4 m below the sea surface.

	S1				S2			
	Tidal		Subtidal		Tidal		Subtidal	
	rms error	r	rms error	r	rms error	r	rms error	r
η (m)	0.16	0.96	0.13	0.65	0.16	0.96	0.14	0.43
$u_{-1.2}$ (cm s^{-1})	3.28	0.78	1.84	0.36	4.58	0.66	2.87	0.52
$v_{-1.2}$ (cm s^{-1})	5.94	0.81	4.71	0.89	5.92	0.73	4.53	0.81
$u_{-4.2}$ (cm s^{-1})	2.21	0.89	1.15	−0.10	2.93	0.83	1.37	0.68
$v_{-4.2}$ (cm s^{-1})	5.27	0.79	4.21	0.86	5.80	0.67	4.95	0.73

variability for each type of storm, at stations B1 and B2, was identified using a phase-averaging method. The time step of each recorded storm event was normalized by its duration and an averaged wind stress value was estimated at each normalized time step. The time-normalized, event-averaged winds showed that (see Figs. 5–7 in Wu et al. 2017) during a CF (WF) event, the wind is initially northward (southward) directed and then rotates clockwise to southward (northward). For the periods corresponding to opposing directions, wind speed first increases and then decreases. During a TS event, the wind is persistently southward, and its speed increases first and subsequently decreases. Following Wu et al. (2017), the time steps corresponding to changes in wind direction during the frontal (i.e., CF and WF) events and when wind speed attains its maximum value during the TS event are used to define the "central point" of each event. This central point separates the developing and decaying phases of the particular event. For the CF and WF events, each phase (i.e., developing/decaying) has a local wind speed maximum, while only a single maximum is present during the TS event. The mean duration is approximately 85, 90, and 72 h, with the standard deviations being 40, 43, and 47 h for the CF, WF, and TS events, respectively.

To simulate the most energetic shelf circulation driven by storms, the wind forcing representing each storm type is reconstructed considering the most intense condition recorded (see Fig. 3, left). The time-normalized, event-averaged wind vectors at each station are converted to a maximum-strength event by multiplying the mean wind speed by a factor. The factor was determined empirically by scaling the two local maxima of wind speed for a CF or WF event and the maximum wind speed for a TS event to the corresponding maximum values ever recorded within the 10-yr study period in Wu et al. (2017).

To isolate the effects of regional (i.e., spatial scale larger than that of the embayment) winds, a comparative wind pattern is also created for each storm type that consists of only the regional alongshore (i.e., along the y axis) wind component (see Fig. 3, right). This 1D (i.e., uniform wind direction over the domain) wind field has a smaller magnitude than the full 2D (i.e., both wind speed and direction vary in space) winds; the wind direction is along the y axis of the domain and is aligned with the isobaths at water depths $h > 20$ m (see Fig. 1b). At shallower water depths, this 1D wind field is at an angle to the curved isobaths and coastline. The normalized time steps are converted into time units by multiplying them by the corresponding mean event duration (Fig. 3). The cross-shore spatial variability of wind velocity across the domain is estimated using Eq. (2.1).

The effects of stratification are examined using two numerical experiments with identical wind forcing (i.e., full 2D or 1D) but with initially well-mixed and stratified shelf conditions. Shelf water climatology at the study area indicates the presence of vertical stratification from late spring to summer and the development of a pronounced cross-shore density gradient in winter (Blanton et al. 2003). Here, only the former condition is considered, and the cross-shore mean of the climatologically defined summer vertical temperature structure is used. This structure consists of three layers (Blanton et al. 2003; Castelao 2011): a surface mixed layer (28°C) extending to 20 m below the sea surface, a colder (22°C) bottom layer (>60 m), and an intermediate layer with a linearly decreasing temperature. For the mixed condition runs, the temperature and salinity were set constant vertically (22°C and 35, respectively) and throughout the domain. The effects of tides and the Gulf Stream are not considered in these simulations. Each simulation started at rest, and the wind speed was ramped up over a period of 24 h.

3. Results

This section presents the general circulation patterns under the full 2D wind forcing of each event. Emphasis is placed on the effects of stratification and the spatial variability of the shelf circulation. Then, these results

Brought to you by NOAA Central Library | Unauthenticated | Downloaded 01/16/24 05:03 PM UTC

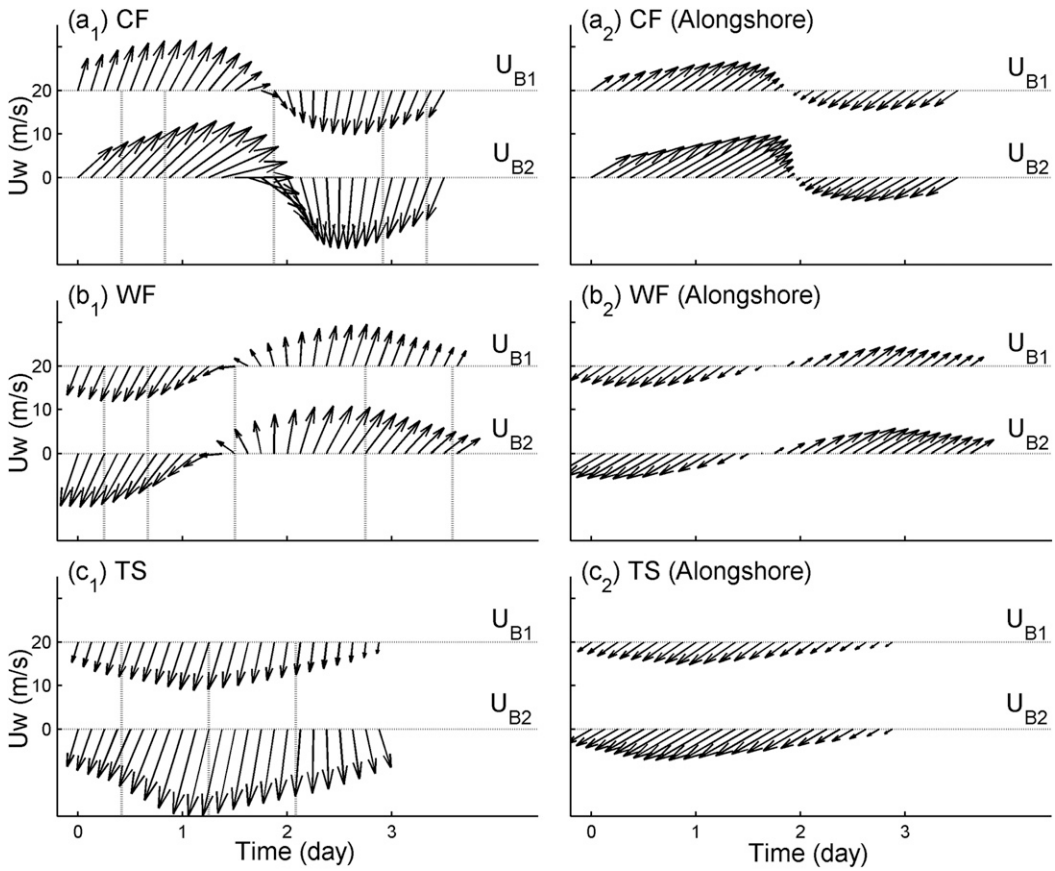

FIG. 3. (left) The original full 2D wind field as defined climatologically at the onshore $\mathbf{U}_{B1}$ and offshore $\mathbf{U}_{B2}$ stations during the (a) CF, (b) WF, and (c) TS events. Vertical lines indicate the time steps corresponding to the results shown in Figs. 4, 5, and 6. (right) The 1D wind field along the regional alongshore direction derived from the 2D wind field.

are compared with the results from the simulations driven by the 1D wind forcing.

a. Event-driven circulation patterns

1) COLD FRONTS

Figure 4 shows the circulation patterns near the sea surface (red vectors) and at midwater depth (black vectors), for both mixed (Fig. 4, left column) and stratified (Fig. 4, center and right columns) conditions and for five different time steps of the CF event. For the stratified conditions, the spatial variability of bottom temperature is also shown in Fig. 4 (center column). The cross-shore and vertical variabilities of cross-shore flow and temperature are shown in Fig. 4 (right column) along a transect in the center of the domain [see white line in Fig. 4a(2)]. The selected time steps correspond to the developing (10 and 20 h) phase, central point (45 h), and decaying (70 and 80 h) phase of the storm [see Fig. 3a(1)]. During the developing phase, the northeastward-directed flow enters the embayment in the south and diverges as a result of isobath diversion. This pattern is present in both barotropic and baroclinic runs [see Figs. 4a(1) and 4b(1) and Figs. 4a(2) and 4b(2)]. Farther downstream, as the flow approaches the northern cusp, it converges and deflects slightly offshore owing to presence of the shoals. During the decaying phase, the wind forcing is downwelling/offshore directed [see wind vector in Figs. 4d(1) and 4e(1)] and the current reverses direction. As the current flows into the embayment from the north, it also experiences divergence and convergence at the northern and southern sides of the embayment, respectively [see Figs. 4d(1) and 4d(2) and Figs. 4e(1) and 4e(2)].

During the developing phase, the near-surface (midwater column) flows under stratified conditions exhibit a more intensified offshore (onshore) flow component than that found under mixed conditions; this is more pronounced in water depths > 40 m [cf. Figs. 4b(1) and 4b(2)]. In shallow waters [$h < 30$ m;

Brought to you by NOAA Central Library | Unauthenticated | Downloaded 01/16/24 05:03 PM UTC

see Figs. 4a(3) and 4b(3)], the initially stratified water column becomes well mixed, while upwelling develops farther offshore ($h > 30$ m). During the decaying phase [Figs. 4d(3) and 4e(3)], the downwelling/offshore winds tend to extend mixing farther offshore, to a water depth of 35 m. In deeper waters ($h > 35$ m), a two-layer downwelling circulation is evident with offshore flows near the bottom [Fig. 4d(3)]. Prior to downwelling [Fig. 4c(2)], the bottom 25°C isotherm (white line) is displaced farther onshore at the southern part of the embayment relative to the northern part. During downwelling [Figs. 4d(2) and 4e(2)], the offshore displacement of the same isotherm is larger at the southern location than that at the northern. These isotherm displacements indicate enhancement of upwelling (downwelling) at the southern part during the developing (decaying) phase. At the central point of the CF event [Fig. 4c(3)], the offshore directed wind velocity component diminishes and the cross-shore currents are offshore directed over the entire water column.

2) WARM FRONTS

The WF simulation results are shown in Fig. 5. In contrast to the CF case, the full 2D wind forcing is downwelling/offshore directed during the developing phase [see Figs. 3b(1) and 5b(1)], and it reverses to upwelling/onshore directed during the decaying phase [see Fig. 5d(1)]. For both mixed and stratified conditions, the flow divergence/convergence patterns described earlier for the CF event are also present here (see Fig. 5, left and center). Under mixed conditions, the simulation results resemble those described in section 3a(1) for the CF event. Under stratified conditions, downwelling (upwelling) develops during the developing (decaying) phase [Figs. 5a(3), 5b(3), and 5d(3)]. Upwelling moves the bottom 25°C isotherm slightly onshore [Figs. 5d(2) and 5e(2)]. In water depths > 30 m, stratification persists for the whole duration of the event. Toward the end of the decaying phase with weakening winds, near-bottom flow in water depths > 30 m is offshore directed [Fig. 5e(3)]; this is opposite to the onshore flows at the previous time step [$T = 66$ h; Fig. 5d(3)].

3) TROPICAL STORMS

The simulated horizontal flows and associated temperature structure under TS forcing are shown in Fig. 6. The circulation patterns driven by downwelling/offshore winds resemble those found during the WF developing phase (see Fig. 5). Under stratified conditions and shortly after the onset of the event, the water column becomes well mixed. This is particularly the case in shallow ($h < 30$ m) waters [see Figs. 6a(2), 6a(3), 6b(2), and 6b(3)]. Current veering in the vertical develops around the central point of the storm, especially at the northern side of the domain [see Figs. 6b(1) and 6b(2)], and it extends to shallow waters ($h < 20$ m). Such veering is also observed during the CF and WF events [see Figs. 4d(2) and 5b(2)] but to a lesser extent. As the currents enter into the embayment from the north, onshore flow develops at and below midwater, while the surface currents are well aligned with the generally alongshore-directed wind forcing.

b. *Cross-shore flows*

The simulated cross-shore currents at the mid-/outer shelf, and for each type of storm, are examined at a single location (site P1) at a water depth of 40 m (see Fig. 1). The simulation results for stratified and mixed conditions are compared in Fig. 7. In the latter case and during the developing stages of both CF and TS (Figs. 7a,e) and the WF run (Fig. 7c), a nearly uniform cross-shore current develops that extends throughout the water column. For initially stratified conditions, a two-layer flow develops during the developing phase of all event types. The CF simulation shows the development of a two-layer cross-shore upwelling circulation (Fig. 7b) during the developing phase. During the initial stage of the decaying phase (hours 42–47) an offshore-directed cross-shore flow develops that persists throughout the water column [as also shown in Fig. 4c(3)]. This is followed by the development of a two-layer downwelling circulation pattern. For the WF simulation, the model results reveal downwelling circulation during the developing phase, and a two-layer upwelling circulation during the decaying phase. A persistent downwelling circulation and a more homogeneous water column are found for the TS simulation. Overall, under stratified conditions, smaller vertical temperature gradients are present for the WF than the CF run, although stratification persists for both events. During the TS simulation, stratification is present only during the developing phase, and the water column becomes well mixed during the decaying phase.

c. *Alongshore variability of upwelling/downwelling*

In addition to the temporal variability, the simulations reveal an alongshore variability of the upwelling/downwelling flow structure [Figs. 4c(2) and 4d(2)]. This is quantified using the horizontal position of the bottom 25°C isotherm. In the CF run, after $T = 45$ h, the wind is downwelling favorable (Fig. 4); however, the near-bottom flow at the southern side of the embayment persists to be onshore directed until $T = 60$ h, the time the bottom 25°C isotherm reaches its farthest onshore position. For the WF run, upwelling flows develop during the last 45 h of the WF event (i.e., $T = 40$–85 h), and the 2D

Brought to you by NOAA Central Library | Unauthenticated | Downloaded 01/16/24 05:03 PM UTC

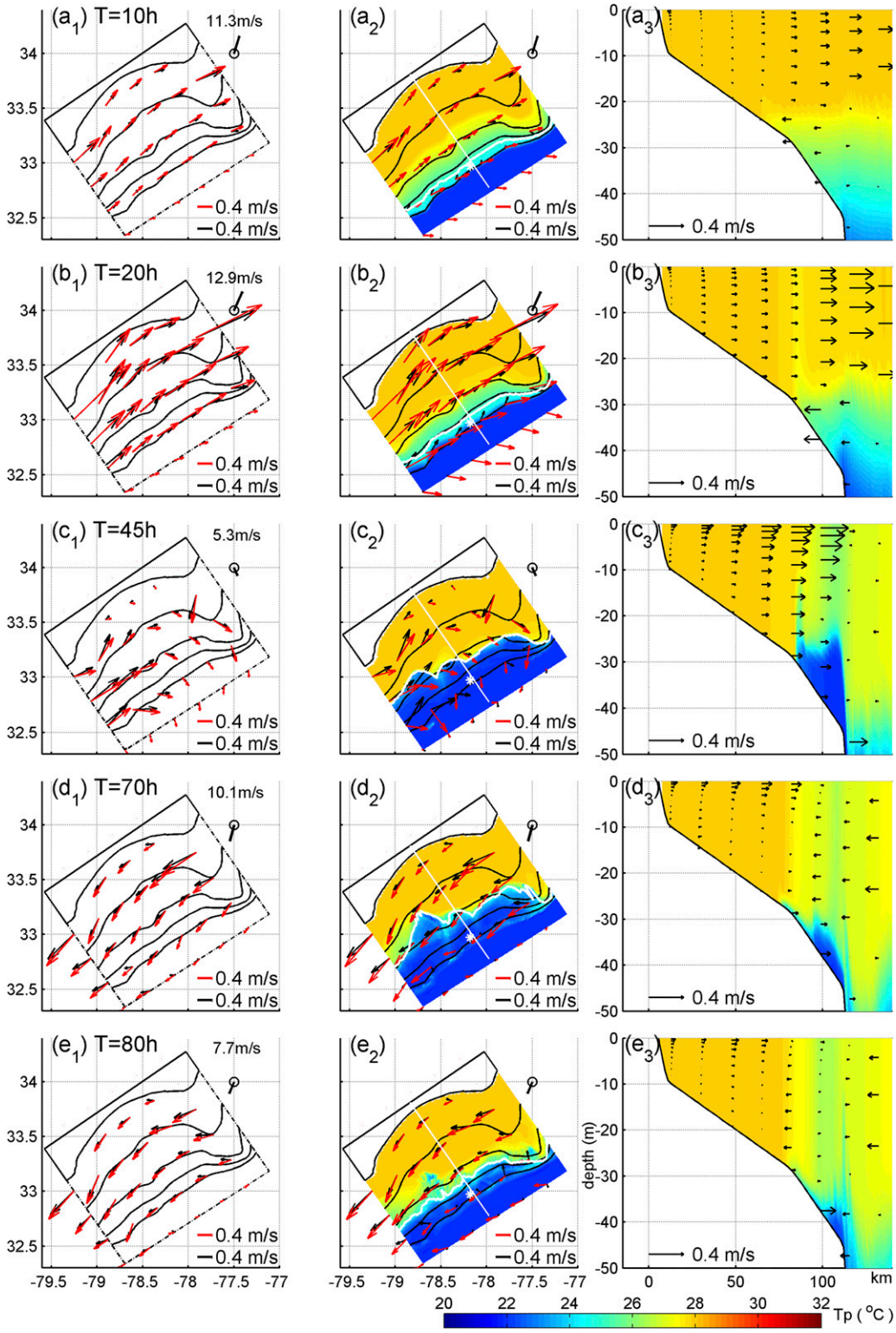

FIG. 4. Spatial and temporal circulation patterns during the CF event at five different time steps [10, 20, 45, 70, and 80 h; see Fig. 3a(1)]. (left) Surface (red) and midwater (black) current vectors under mixed conditions. (center) As in the left panels, but for stratified conditions; near-bed sea temperature is also shown (filled color) with the white contour denoting the 25°C isotherm. (right) Cross-shore and vertical variability of cross-shore velocity (vectors) and water temperature along a transect in the middle of the embayment (for location see white

Brought to you by NOAA Central Library | Unauthenticated | Downloaded 01/16/24 05:03 PM UTC

wind forcing is primarily upwelling/onshore directed [see Fig. 3b(1)]. Downwelling flows develop during the last 20 h (T = 60–80 h) of the CF event, a period dominated by regional downwelling/offshore-directed winds [Fig. 3a(1)]. Figure 8 shows the horizontal positions of the bottom 25°C isotherm at selected time steps (solid lines). Displacement of the isotherm can be attributed to (i) downstream advection in the alongshore direction, (ii) wind-induced upwelling (or downwelling), and (iii) topographically induced cross-shore flows. The cross-shore displacement induced by the latter two components is revealed after compensating for alongshore advection. The shape of the bottom 25°C isotherm (defined by its x, y coordinates) is compared at selected time steps using cross-correlation analysis. The alongshore distance lag Δy, corresponding to the highest correlation, is used to define the alongshore displacement of the isotherm due to advection within the period ΔT between two adjacent time steps. The isotherm is then shifted in the alongshore by this distance, and the net cross-shore displacement of the isotherm is estimated.

During the CF upwelling phase, isotherm alongshore displacements of 4.2 and 8.2 km are estimated for the first (i.e., 0–30 h) and second half (i.e., 30–60 h) of the 60-h period, respectively [Fig. 8a(1)]. The corresponding values for upwelling during the WF simulation are 0.8 (for 40–60 h) and 1.6 km (for 60–85 h), respectively [Fig. 8b(1)]. Using the compensated isotherm positions [Figs. 8a(2) and 8b(2)], differences in upwelling intensity at three locations (y = 44, 104, and 164 km) representing the southern, middle, and northern parts of the embayment are estimated. For the CF upwelling, the isotherm displacements in the onshore direction are 52.4, 18.7 and 4.7 km, respectively. The corresponding displacements during the WF upwelling phase are 14.5, 12.2, and 4.4 km. This larger isotherm displacement at the southern side suggests that upwelling is promoted there, while the relatively smaller displacement at the northern side suggests an inhibition of the upwelling.

For downwelling, the cross-shore (offshore) displacements of the isotherm are 39.2, 7.1, and 3.2 km at the southern, middle, and northern locations, respectively [Fig. 8c(2)]. Thus, downwelling is seemingly promoted at the southern site. However, in this case the effect of wind-induced mixing becomes important (see below).

In an attempt to further isolate the effects of the regionally defined cross-shore wind component, the results from the full 2D (Fig. 3, left) and the regionally defined 1D wind (Fig. 3, right) fields are compared. The positions of the bottom 25°C isotherm in the latter runs are shown in Fig. 8 as dashed lines. In deep waters ($h >$ 20 m), the isobaths are relatively straight and no cross-shore wind component is present during the 1D wind forcing runs. During the first 30 h of the CF run, the isotherm locations for the 2D and 1D runs are similar [Fig. 8a(2)]. However, during the following 30 h, as the isotherm enters into water depths $<$ 30 m, the regional, offshore-directed wind component in the 2D wind forcing appears to promote the onshore advancement of the isotherm along the entire coastline. This result is consistent with the findings of Horwitz and Lentz (2016) that, in the inner shelf, upwelling/offshore-directed winds promote stratification and cross-shore transport. During the CF downwelling phase [Fig. 8c(2)], the downwelling/offshore-directed winds result in a much larger cross-shore retreat of the isotherm. This is expected, as the wind-induced mixing under such conditions is more intense than that under 1D (i.e., purely alongshore directed, downwelling favorable) wind forcing. During the downwelling and subsequent upwelling [Fig. 8b(2)] phases of the WF event, the 25°C isotherm remains at the same location for these two wind forcing conditions. This is also the case during the TS downwelling phase. These results are attributed to the well-mixed conditions of the inner shelf ($h <$ 30 m) and the negligible effects of the regional cross-shore wind component.

4. Discussion

The simulation of the CF event revealed an alongshore variability in the intensity of the upwelling/downwelling circulation. This alongshore variability is investigated here. In addition, the change of coastline orientation in the alongshore contributes to the development of a locally defined cross-shore wind component, the effect of which is discussed below.

a. Momentum balance analysis

To better understand the enhanced upwelling at the southern embayment, the momentum balance diagnostics are first presented. The three-dimensional

←

line in center panels). The 20-, 30-, 40-, and 50-m isobaths are shown as black contours. Wind forcing at each time step is shown as a velocity vector on the upper right of the model domain. The white star (center column) marks the location of site P1 (see section 3b).

Brought to you by NOAA Central Library | Unauthenticated | Downloaded 01/16/24 05:03 PM UTC

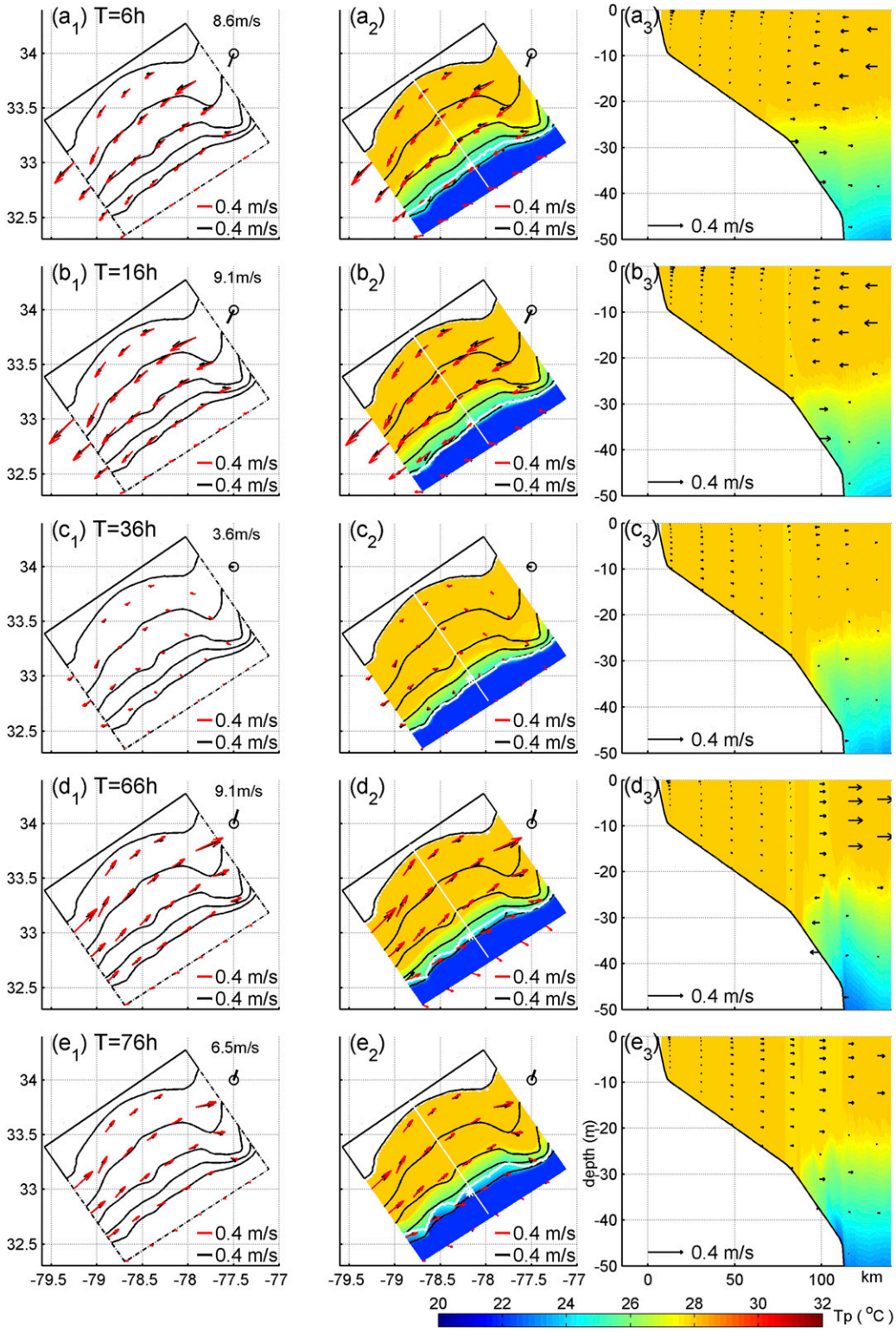

FIG. 5. As in Fig. 4, but for the WF event. The time steps shown correspond to 6, 16, 36, 66, and 76 h since the onset of the WF event [see Fig. 3b(1)].

Brought to you by NOAA Central Library | Unauthenticated | Downloaded 01/16/24 05:03 PM UTC

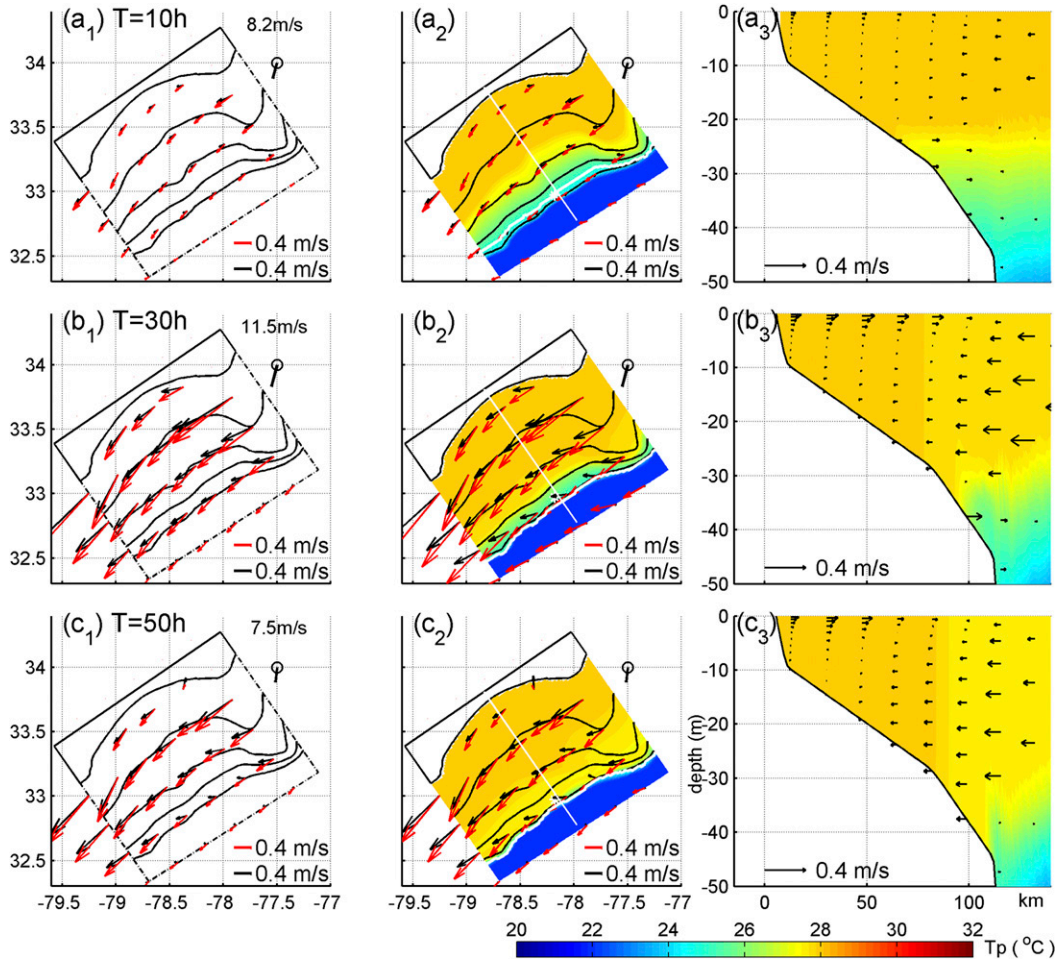

FIG. 6. As in Fig. 4, but for the TS event. The time steps shown correspond to 10, 30, and 50 h since the onset of the event [see Fig. 3c(1)].

momentum balance along the x and y directions can be expressed as follows:

$$\frac{\partial u}{\partial t}+\left(u\frac{\partial u}{\partial x}+v\frac{\partial u}{\partial y}+w\frac{\partial u}{\partial z}\right)=-\frac{1}{\rho}\frac{\partial p}{\partial x}+fv+\frac{\partial}{\partial z}\left(K_m\frac{\partial u}{\partial z}\right),$$

and (4.1)

$$\frac{\partial v}{\partial t}+\left(u\frac{\partial v}{\partial x}+v\frac{\partial v}{\partial y}+w\frac{\partial v}{\partial z}\right)=-\frac{1}{\rho}\frac{\partial p}{\partial y}-fu+\frac{\partial}{\partial z}\left(K_m\frac{\partial v}{\partial z}\right), \quad (4.2)$$

where w is the vertical current component, ρ is the water density, p is total pressure, and K_m is the vertical eddy viscosity. The two terms on the LHS of each equation represent local acceleration (LA) and advective acceleration (AA), while the three terms on the RHS are the pressure gradient (PG), Coriolis forcing (CA), and vertical mixing (VM), respectively.

In the cross-shore direction the balance is predominantly geostrophic at water depths > 20 m, consistent with previous results (Lee et al. 1989; Lentz et al. 1999) and is not shown here. The alongshore y variability of the alongshore momentum balance terms is examined along an alongshore transect located at approximately 40-m depth, an area with relative straight isobaths. The spatial variability of the terms along the transect from the CF event simulation, under the full 2D wind forcing is shown in Fig. 9 for $T = 30$ h. Although this time step is arbitrarily selected, the results are representative for the entire event. The analysis reveals that the balance is primarily between VM and the sum of CA and PG (Figs. 9c,d,e). The term AA has notable contribution at the southern ($y < 50$ km) and northern (140 km $< y <$ 160 km) parts of the embayment, while within the embayment (50 km $< y <$ 140 km) it is less important (Fig. 9b). LA is insignificant over the entire shelf and not shown in Fig. 9. Both CA and VM terms

Brought to you by NOAA Central Library | Unauthenticated | Downloaded 01/16/24 05:03 PM UTC

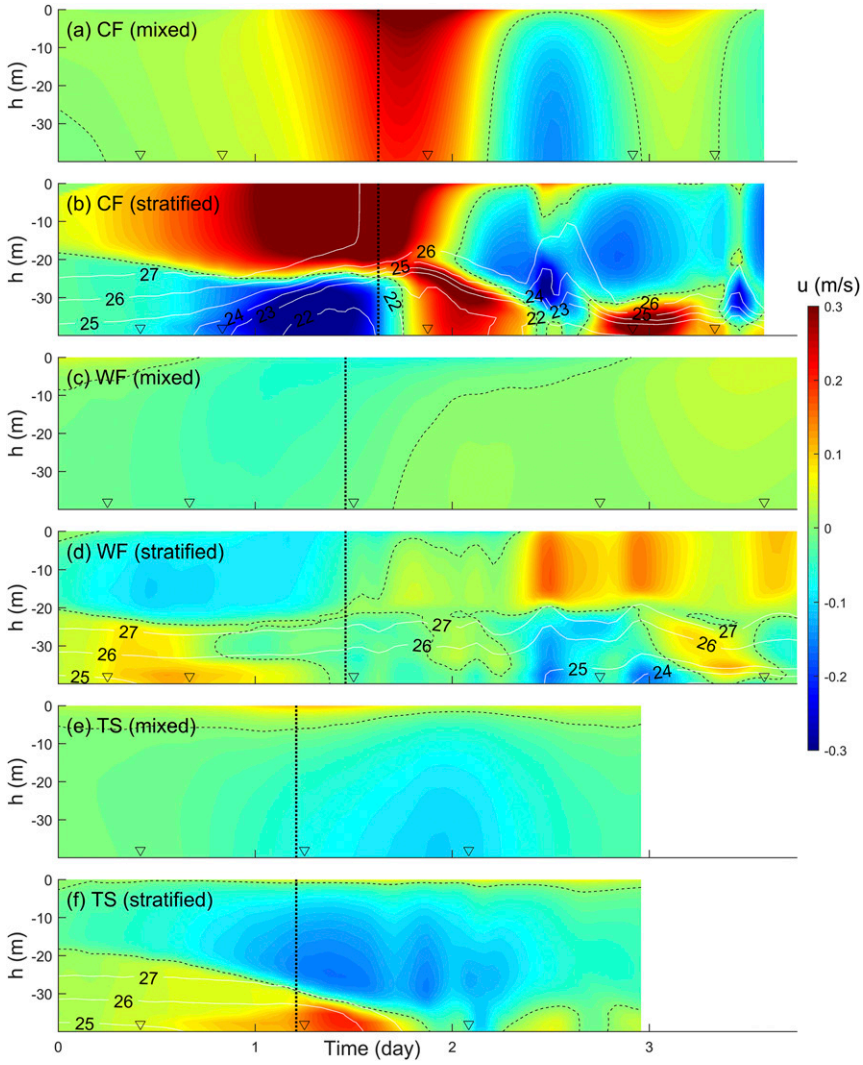

FIG. 7. Temporal evolution of cross-shore velocity u (filled colors) and temperature (contours) at site P1 (for location, see Fig. 1) for the CF, WF, and TS events. Simulation results (a),(c),(e) under mixed conditions and (b),(d),(f) under stratified conditions. The vertical line corresponds to the central point of each event, while the triangles mark the time steps shown in Figs. 4, 5, and 6.

change signs within the surface and bottom boundary layers (Figs. 9c,e). The alongshore PG has a larger magnitude in locations with $y < 60$ km, and it balances the alongshore CA at depth within this area (Fig. 9d). The alongshore momentum balance pattern described above also holds in shallower waters (i.e., ~30 m; not shown here). The balance between alongshore PG and CA at depth was also reported for simulations indicating enhanced upwelling downstream of capes (Gan and Allen 2002). However, the gradual increase in the downstream sea level (Fig. 9a) was not identified in Gan and Allen (2002), and instead a local sea level minimum was revealed at the cape location.

Farther onshore in the region where the isobaths start curving (i.e., $h < 20$ m), the water is well mixed. In the cross-shore direction (defined as the normal to the bathymetric contours; same as that used in section 2b), in addition to the CA and PG terms, the VM (not shown here) associated with the locally defined cross-shore wind component becomes important because of the alongshore variation of the coastline orientation. This is particularly the case at the northern part of the domain (where the 2D CF winds are more aligned with the local cross-shore direction). The alongshore variability of the cross-shore PG and its relation to the local along-/cross-shore wind stress are further discussed in section 4c.

Brought to you by NOAA Central Library | Unauthenticated | Downloaded 01/16/24 05:03 PM UTC

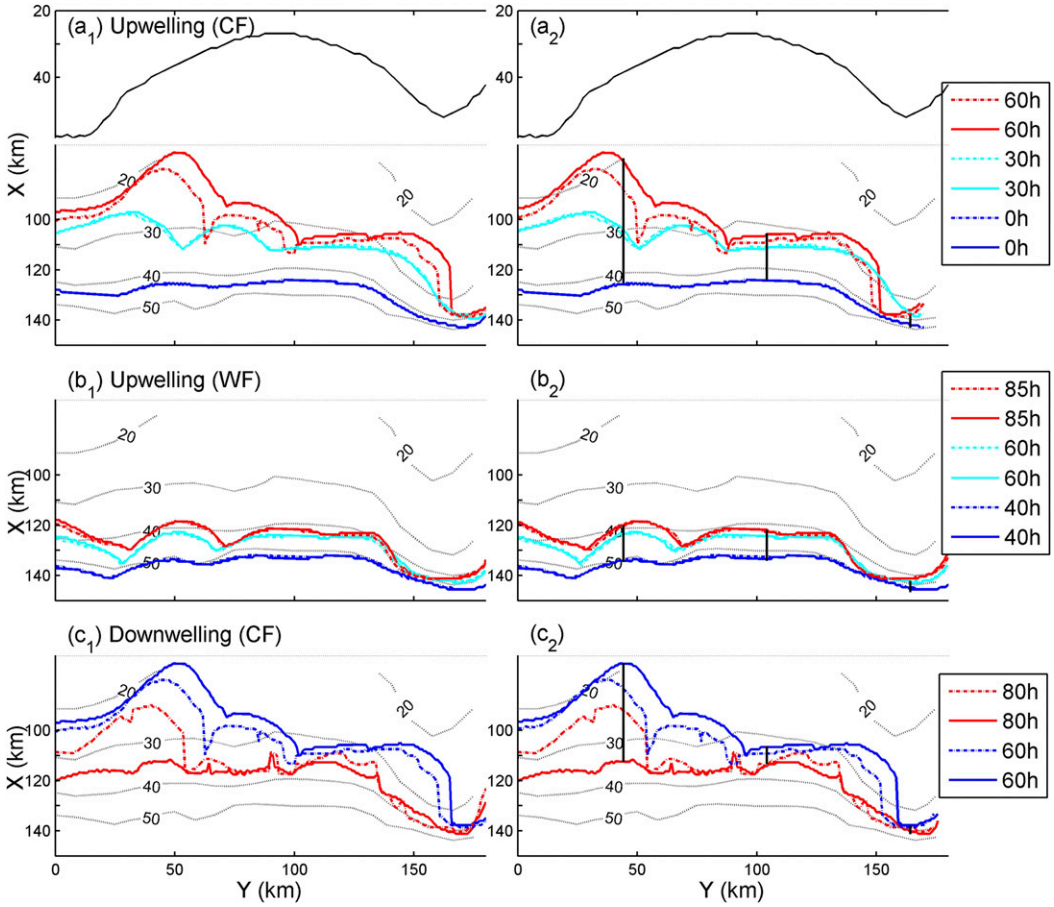

FIG. 8. (left) Position of bottom 25°C isotherm at specific time steps (for times see legends) during the upwelling phase of the (a) CF and (b) WF events and (c) downwelling phase of the CF event. (right) As in the left panels, but with the alongshore y position of the isotherm displaced to account for alongshore advection (see section 3c). Solid and dashed lines denote simulations driven by the full 2D and regionally defined 1D wind forcing, respectively. The bathymetry (contours) and the coastline (black line) are shown for reference. The three vertical lines in the right panels show the net cross-shore displacements of the isotherm at those locations.

b. Cross-shore transport

Pringle (2002) has shown that alongshore variation of shelf width affects wind-driven circulation. For example, a downstream widening shelf, when subjected to upwelling favorable wind forcing, experiences enhanced onshore flow within the bottom layer at the wider side of the shelf. In the case of downwelling, the same study showed that the offshore flow within the bottom layer is inhibited on the wider side of the shelf. In our case, the morphology of the embayment leads to a widening and narrowing of the shelf with the maximum width being attained in the middle of the embayment. Following the approach used in Pringle (2002), we quantify cross-shore transport using the depth integrated shallow water equations:

$$\frac{\partial U}{\partial t}+\left(U\frac{\partial U}{\partial x}+V\frac{\partial U}{\partial y}\right)=-g\frac{\partial \eta}{\partial x}+fV+\frac{\tau^{sx}}{\rho h}-\frac{\tau^{bx}}{\rho h},$$

and (4.3)

$$\frac{\partial V}{\partial t}+\left(U\frac{\partial V}{\partial x}+V\frac{\partial V}{\partial y}\right)=-g\frac{\partial \eta}{\partial y}-fU+\frac{\tau^{sy}}{\rho h}-\frac{\tau^{by}}{\rho h}, \quad (4.4)$$

where (U, V) are the cross- and alongshore components of the depth-averaged current velocity, (τ^{sx}, τ^{sy}) and (τ^{bx}, τ^{by}) are the two components of surface $\boldsymbol{\tau}^s$, and bottom $\boldsymbol{\tau}^b$ stress, respectively. In the equations above, the baroclinic pressure gradient has been ignored. Here, an orthogonal, rather than a curvilinear (Pringle 2002), coordinate system is used to be consistent with the model coordinate system. Using Eqs. (4.3) and (4.4) the potential vorticity equation is derived, and after

Brought to you by NOAA Central Library | Unauthenticated | Downloaded 01/16/24 05:03 PM UTC

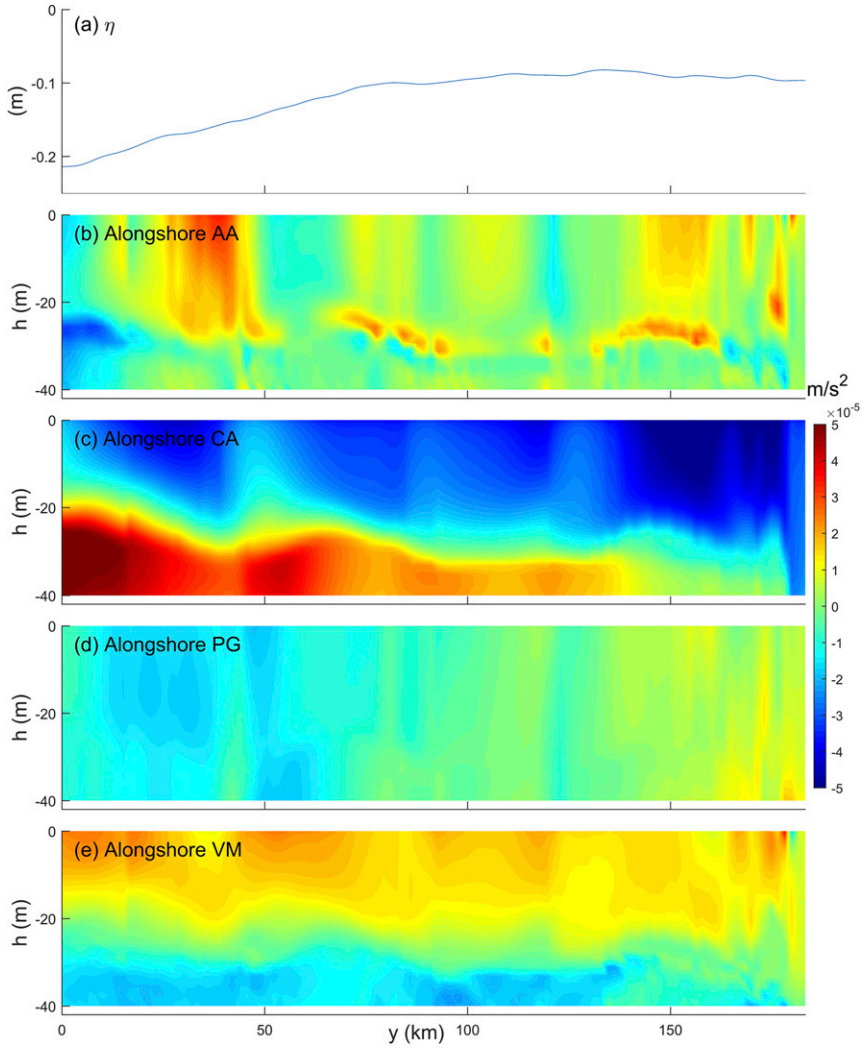

FIG. 9. Alongshore variability of (a) surface sea level and vertical structures of alongshore (b) AA, (c) CA, (d) PG, and (e) VM at $T = 40$ h during the CF event and along the 40-m isobath.

rearranging the terms, the cross-shore (x direction) transport can be estimated using

$$Q_x = \left[\frac{\partial}{\partial x}\left(\frac{f}{h}\right)\right]^{-1}\left[\nabla\times\frac{\boldsymbol{\tau}^s}{\rho h} - \nabla\times\frac{\boldsymbol{\tau}^b}{\rho h} - Q_y\times\frac{\partial}{\partial y}\left(\frac{f}{h}\right) - \frac{\partial}{\partial t}(\nabla\times\mathbf{U}) - \nabla\times\mathbf{A}_\Sigma\right], \tag{4.5}$$

where Q_x and Q_y are the depth-integrated cross-shore and alongshore transport components and $\mathbf{A}_\Sigma(=U\partial U/\partial x + V\partial U/\partial y,\ U\partial V/\partial x + V\partial V/\partial y)$ is the nonlinear term. The first two terms on the rhs of Eq. (4.5) represent surface (Q_{ES}) and bottom (Q_{EB}) Ekman transport, respectively. The third term represents the geostrophic transport (Q_{GS}), and it develops over the entire water column. In a curvilinear isobath-following coordinate system (e.g., Pringle 2002) Q_{GS} would become zero. As our analysis is based on an orthogonal coordinate system, this term is nonzero because of a nonzero alongshore shelf slope $\partial h/\partial y$. The fourth term (hereafter denoted as Q_{LA}) is induced by the local change of relative vorticity, while the last term is associated with horizontal advection (hereafter denoted as Q_{AA}). All terms of Eq. (4.5) are estimated using the model diagnostics.

Figure 10 shows the planar distribution of each term averaged over the first 30 h during the upwelling stage of the 2D CF run. The first 30 h correspond to a period when the effect of the regional cross-shore wind component is found to be insignificant (see Fig. 8 and section 3c). The Q_x and Q_y are calculated from the simulated cross-shore and alongshore velocity components, respectively, while Q_{LA} is combined with Q_{AA} as the former is much smaller than the latter. The fine-scale variability (see contours in Figs. 10b–f) may be

Brought to you by NOAA Central Library | Unauthenticated | Downloaded 01/16/24 05:03 PM UTC

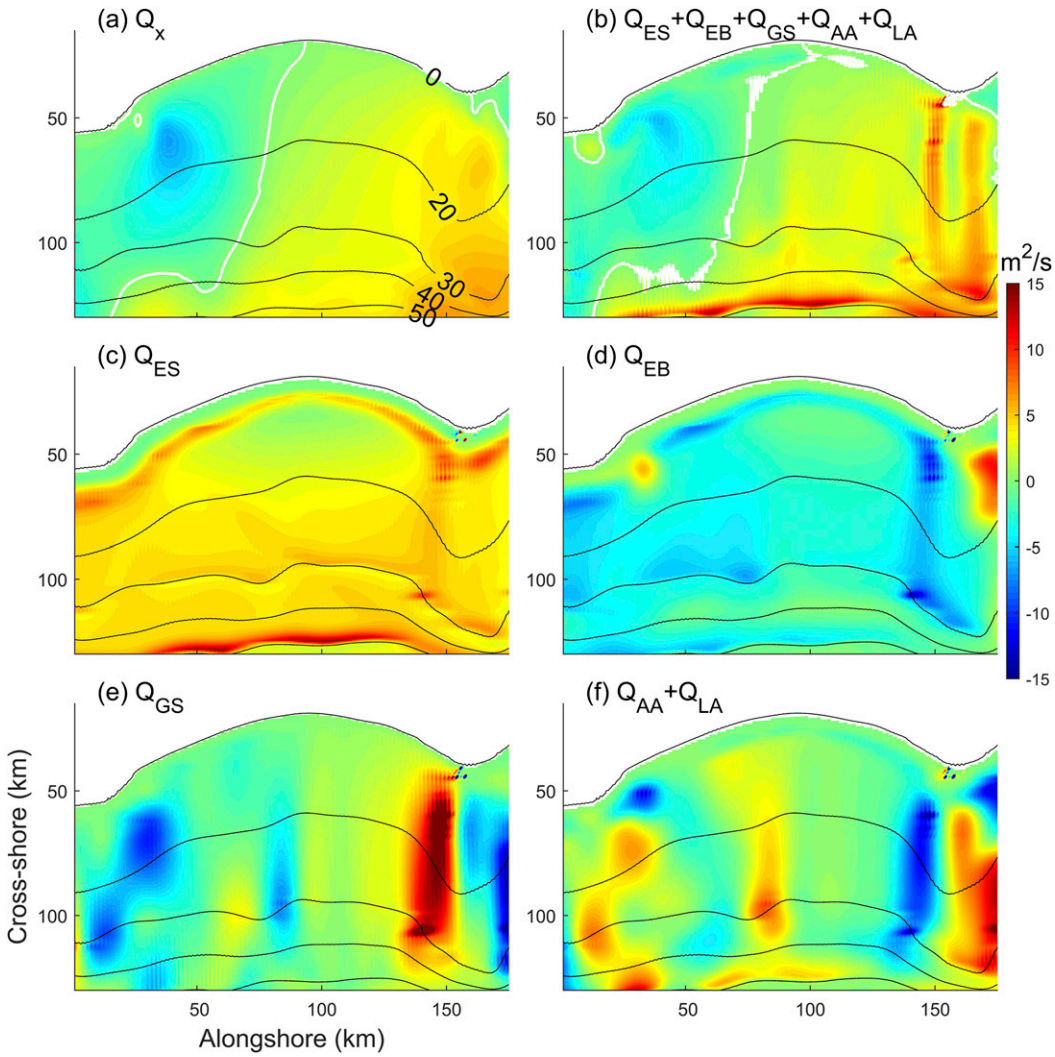

FIG. 10. Horizontal distribution of the simulated (a) net cross-shore transport Q_x; (b) the sum of Q_{ES}, Q_{EB}, Q_{GS}, Q_{AA}, and Q_{LA}; (c) Q_{ES}; (d) Q_{EB}; (e) Q_{GS}; and (f) the sum of Q_{AA} and Q_{LA}. The white line in (a) and (b) denotes the $0\,m^2\,s^{-1}$ contour. All terms are averaged over the first 30 h of the CF event. The isobaths are shown as black contours (m).

attributed to local bathymetric variations. In the downstream (from left to right in Fig. 10) direction, the net cross-shore transport Q_x changes from negative (shoreward) to positive (seaward) values (Fig. 10a), indicative of the enhanced upwelling (i.e., relatively strong near-bottom onshore flow) seen at the southern side of the embayment. In Pringle (2002), the bottom Ekman transport Q_{EB} decreases as the shelf widens in the downstream direction. Here, no obvious alongshore change of Q_{EB} is found within the embayment (Fig. 10d). This is possibly due to the subtle change of the shelf width (i.e., from 90 km at the southern side to 102 km at the middle of the embayment). The geostrophic transport Q_{GS} is spatially variable (Fig. 10e); it is primarily negative (shoreward) for $y < 90$ km, and it becomes positive (seaward) for $110\,\text{km} < y < 150\,\text{km}$. The Q_{GS} is largely compensated by Q_{AA} (Figs. 10e,f), and overall Q_x is well reproduced by the sum of Q_{ES}, Q_{EB}, Q_{GS}, and Q_{AA} (Figs. 10a,b). We speculate that, under upwelling conditions, the enhanced onshore-directed near-bottom flow at the southern embayment is primarily caused by the onshore geostrophic transport Q_{GS} and the response term Q_{AA}. This is supported by the higher alongshore PG seen at the region $y < 60$ km, when compared with that at $y > 60$ km (see Fig. 9d). This higher PG value is balanced by the alongshore CA at depth that is associated with the near-bottom onshore flow. Under the downwelling period of the CF (or WF) run, Q_{AA} also has notable contribution. The main differences are as follows:

Brought to you by NOAA Central Library | Unauthenticated | Downloaded 01/16/24 05:03 PM UTC

1) moving from the southern to northern parts of the embayment, Q_x shifts from positive (seaward) to negative (shoreward), and 2) the sign of Q_{ES} reverses as the alongshore transport Q_y reverses [see Eq. (4.5)]. The near-bottom downwelling flow displaces the bottom 25°C isotherm offshore, and no onshore displacement of the isotherm is seen at the northern side of the embayment, even though the geostrophic transport Q_{GS} is shoreward at this location. The offshore flows over the entire water column, shown in Figs. 4c(3) and 5e(3) during the weakening of the wind forcing, most likely, are related to the terms Q_{GS} and Q_{AA}.

c. *Alongshore variation of cross-shore pressure gradient and sea level*

Given a constant wind forcing on a curved coastline, the locally defined along- and cross-shore wind velocity components will vary spatially, leading to a spatially varying local cross-shore pressure gradient and corresponding sea level. In an attempt to quantify the spatial variability of the local along-/cross-shore wind stress, the temporal variation of cross-shore PG and sea level and their correlations with wind stress are investigated. Following Tilburg (2003), the local cross-shore PG ($\partial P/\partial n$, where $P = g\eta$; n is the direction normal to the isobath and positive seaward) can be decomposed into two parts (denoted as $\partial P_{LA}/\partial n$ and $\partial P_{LC}/\partial n$, respectively) that represent the response to the local along- and cross-shore components of wind stress separately. If the cross angle between the local isobath and wind vector is denoted as θ ($0 \le \theta < 2\pi$, with $\theta = 0$ for upwelling-favorable winds and $\pi/2$ for onshore-directed winds), then using simple geometrical arguments, we can assume that $\partial P_{LA}/\partial n$ and $\partial P_{LC}/\partial n$ are proportional to the local cross-shore component of Coriolis forcing and the cross-shore wind stress, respectively. Following Tilburg (2003), these relationships can be expressed as follows:

$$\frac{\partial}{\partial n}P_{LA}(T) = -\alpha_0 f V_c(T - \Delta T_{LA}) = -\alpha_{LA} f \cos\theta U_w(T - \Delta T_{LA}), \quad \text{and} \tag{4.6}$$

$$\frac{\partial}{\partial n}P_{LC}(T) = \alpha_{LC}\frac{\sin\theta}{\rho_0 h}\tau^s(T - \Delta T_{LC}), \tag{4.7}$$

where α_0, α_{LA}, and α_{LC} are coefficients of proportionality (>0); V_c is the along-isobath current velocity, and it is assumed to be proportional to the alongshore wind velocity [$V_c = (\alpha_{LA}/\alpha_0)U_w \cos\theta$; e.g., Weber 1983]; ΔT_{LA} and ΔT_{LC} are the time lags (>0) between wind forcing and the corresponding cross-shore pressure gradient components.

The coastal sea level can be calculated after integrating $\partial P/\partial n$ in the cross-shore direction. Here, along a curved coastline, we assume that sea level variation is driven by local alongshore and cross-shore wind components that act close to the curved coastline and by the regional alongshore wind component that acts in the offshore region where the effect of coastline orientation is not important. A background sea level is set up by the regional alongshore wind, while the local wind components induce more variability along the coastline. The cross-shore pressure gradient induced by the regional alongshore wind, denoted as $\partial P_{RA}/\partial n$, can be expressed as

$$\frac{\partial}{\partial n}P_{RA}(T) = -\alpha_{RA} f \cos\theta_1 U_w(T - \Delta T_{RA}), \tag{4.8}$$

where α_{RA} is a coefficient of proportionality (>0) and θ_1 is the cross angle between the wind vector and the y axis. In the following analysis, α_{RA} and the time lag ΔT_{RA} in Eq. (4.8) are considered to be the same as α_{LA} and ΔT_{LA}, respectively. By integrating Eqs. (4.6), (4.7), and (4.8) in the cross-shore direction, the resulting sea level can be expressed as follows:

$$\eta(T) = \frac{\beta_{LA}}{g}\frac{\partial P_{LA}}{\partial n} + \frac{1}{g}\int_0^{\beta_{LC}}\frac{\partial P_{LC}}{\partial n}\,dn + \frac{\beta_{RA}}{g}\frac{\partial P_{RA}}{\partial n}$$
$$= \frac{-f\alpha_{LA}}{g}(\beta_{LA}\cos\theta + \beta_{RA}\cos\theta_1)U_w(T - \Delta T_{LA}) + \frac{1}{g}\int_0^{\beta_{LC}}\alpha_{LC}\frac{\sin\theta}{\rho_0 \times (h_0 + s \times n)}\tau^s(T - \Delta T_{LC})\,dn, \tag{4.9}$$

where β_{LA}, β_{LC}, and β_{RA} represent the cross-shore length scales the corresponding wind components act on; h_0 (=8 m) denotes the water depth along a chosen isobath, and s ($=3 \times 10^{-4}$) is the mean shelf slope. The regional alongshore PG [Eq. (4.8)] is constant over the shelf. Here we neglect the cross-shore variation of θ, and the local alongshore PG [Eq. (4.6)] is assumed to be constant in the cross-shore direction. Along a straight coastline, β_{LA} is zero and β_{RA} represents the cross-shore length scale that the alongshore wind component acts

Brought to you by NOAA Central Library | Unauthenticated | Downloaded 01/16/24 05:03 PM UTC

on. The sum of β_{LA} and β_{RA} represents the cross-shore scale over which both coastline curvature and alongshore wind component affect the shelf dynamics.

A least squares linear-fitting analysis is conducted using the wind forcing at the central site P2 (see Fig. 1 for location), the simulated cross-shore PG, and the simulated sea surface level along the 8-m isobath. Unlike Tilburg (2003), here the sea surface level at the shelf edge is not considered to be zero, and β_{LA}, β_{LC}, and β_{RA} are calculated from the least squares fitting. The sum of Eqs. (4.6) and (4.7) and Eq. (4.9) are first normalized using typical values of the cross-shore PG and sea surface level (i.e., $5 \times 10^{-5}\,\mathrm{m\,s^{-2}}$ and 0.3 m, respectively). The least squares fitting analysis then minimizes the fitting error that can be expressed as

$$\mathrm{Error} = \sum\left\{\left[\left(\frac{\partial P}{\partial n}\right)'_m - \left(\frac{\partial P}{\partial n}\right)'_f\right]^2 + (\eta'_m - \eta'_f)^2\right\}, \quad (4.10)$$

where the prime denotes normalized values, and the subscripts m and f denote simulated and fitted values, respectively. The results of this regression analysis are $\alpha_{LA} = 0.03$, $\alpha_{LC} = 0.60$, $\beta_{LA} = 16.97$ km, $\beta_{LC} = 27.34$ km, $\beta_{RA} = 80.06$ km, $\Delta T_{LA} = 7$ h, and $\Delta T_{LC} = 3$ h, with an overall correlation coefficient $r = 0.88$. The rms errors of the fitting are $1.68 \times 10^{-5}\,\mathrm{m\,s^{-2}}$ and 8.3×10^{-2} m for the cross-shore PG and sea surface level, respectively.

The temporal and alongshore variability of both simulated and fitted cross-shore PG, along the 8-m isobath, is shown in Fig. 11 for each type of storm. The distance Ys, along the 8-m isobath, increases from zero at the southwestern end of the embayment (Fig. 1b) to 122 km at the northeastern end. Identical results are found for the runs under initially stratified conditions as the region in shallow water depths like along the 8-m isobath is always well mixed. The horizontal stripes in the simulated results (Figs. 11a,c,e) are local perturbations due to the alongshore nonuniform bathymetry. It can be seen that the temporal variability of the cross-isobath pressure gradient along the isobath and for each simulation is well captured by the sum of Eqs. (4.6) and (4.7).

Figure 12 shows the temporal and spatial (along the 8-m isobath) variability of the sea level for each storm type under mixed conditions. During the CF event (Fig. 12a), a water level set down develops initially; subsequently as the wind reverses it converts to a setup. A reversed pattern of sea level variability is seen under WF forcing (Fig. 12c). During the TS event, a sea level setup develops (Fig. 12e). Similar spatiotemporal variation of the surface sea level is revealed by Eq. (4.9), as shown in Fig. 12. The time lag between sea level and alongshore wind component is larger than that with the local cross-shore wind component indicating a faster response to this local forcing. On spatial scales, the regional alongshore wind component influences shelf circulation over larger cross-shore distances than the local along-/cross-shore wind component. The sum of β_{LA} and β_{LC} (≈ 97 km) is close to the distance from the coastline to the shelf edge [≈ 102 km; along the central transect shown in Fig. 4a(3)]. The scales over which the local cross-shore wind component acts can reach a water depth of 17 m. We suggest that the individual values of β_{LA} or β_{LC}, as defined, depend on coastline curvature, and possibly the degree of stratification within the inner shelf. However, additional work is required to develop a theoretical framework for explaining the precise role and dependences of these parameters.

d. *Storm-driven shelf circulation*

The temporal variation of wind forcing, as represented through our climatically defined forcing, is critical to better quantify cross-shore circulation. In particular, our results suggest that from the three storm events, it is only during a CF event that the regional cross-shore wind becomes important. The offshore-directed wind component promotes upwelling during the CF developing phase, as the inner shelf ($h < 30$ m) becomes stratified [see Figs. 8a(1) and 8a(2)], while during the decaying phase it enhances vertical mixing. For the WF and TS events, the inner shelf is always well mixed and the effects of cross-shore winds are hardly detectable.

Although the effects of tidal forcing on cross-shore circulation are not considered in this work, regional studies in the SAB have shown that tides contribute substantially to both the along- and cross-shore shelf current variabilities (Blanton et al. 2004) and that they can increase mixing (Castelao et al. 2010; Suanda et al. 2017). Inclusion of tidal stirring may change the position of the 25°C isotherm near the bed and weaken the intensity of the cross-shore flows presented here, but the main patterns might not change significantly.

The storm forcing used in this study represents the most severe conditions; thus, the simulated shelf stratification conditions might not reflect those described in the mean climatology. In addition, only the climatologically defined summer stratification on the SAB has been used in this study. Under realistic conditions a wider range of variability is expected that will depend on river discharge, solar radiation, and position of the Gulf Stream. For instance, a two-layer flow under stratified conditions was observed in the spring, under weak/moderate wind forcing, on the inner shelf

Brought to you by NOAA Central Library | Unauthenticated | Downloaded 01/16/24 05:03 PM UTC

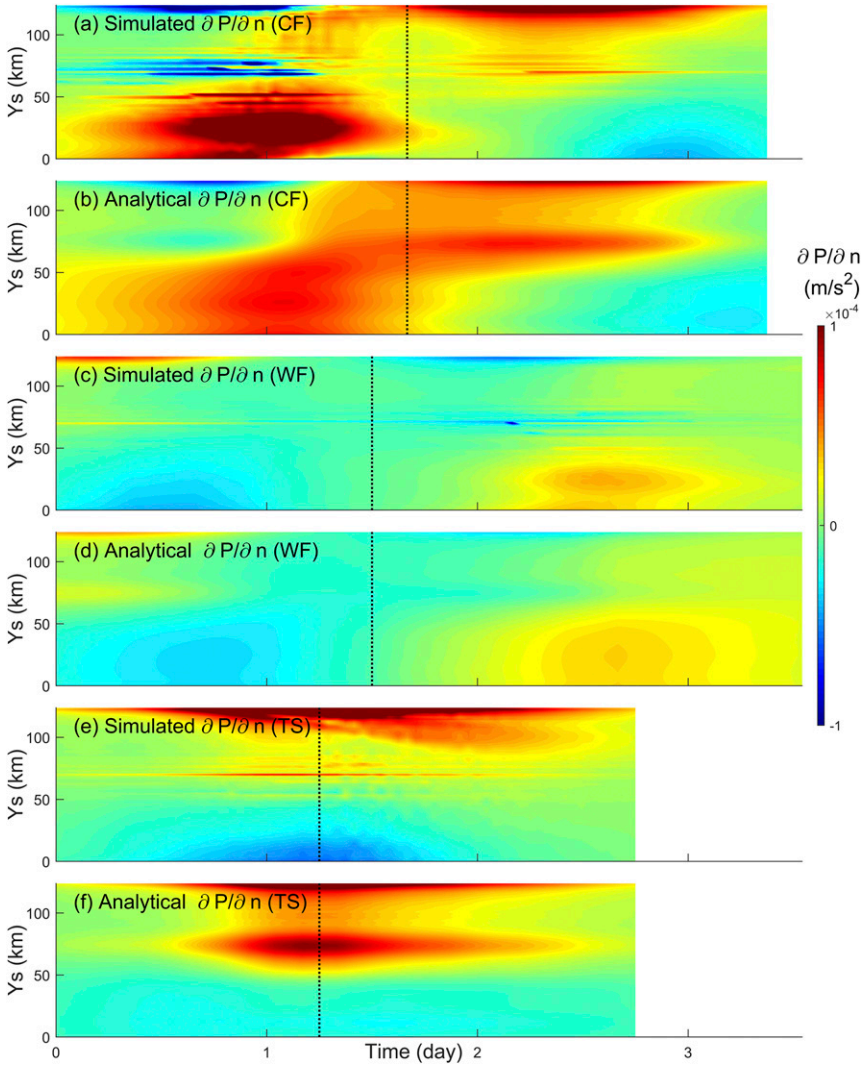

FIG. 11. Alongshore and temporal variability of (a),(c),(e) simulated and (b),(d),(f) analytical cross-shore pressure gradient $\partial P/\partial n$ along the 8-m isobath for the CF, WF, and TS events, respectively. The vertical line identifies the central point of each storm. The Ys is the alongshore distance along the entire concave coastline starting from the southwestern endpoint as shown in Fig. 1b.

at a depth of 12 m of the study site (Gutierrez et al. 2006). A typical stratification observed on the SAB by Austin and Lentz (2002) was characterized by a strong pycnocline present at water depths 8–12 m that was developed underneath the surface mixed layer. Although all these circumstances have not been considered in this work, the general mechanisms described in here are expected to be valid.

5. Summary and conclusions

Responses of the shelf to the three types of storms occurring in the SAB were simulated using a numerical model under both mixed and stratified shelf conditions. Our analysis has shown that persistent upwelling-favorable winds during the cold front (CF) stratify the inner shelf; the presence of a regional offshore-directed wind component promotes upwelling during the developing phase and enhances mixing during the decaying phase of the event. Under warm front (WF) and tropical storm (TS) conditions, this regional cross-shore wind component becomes insignificant as the inner shelf is always well mixed. In an orthogonal coordinate system, net cross-shore transports are induced at the southern and northern sides of the embayment. Besides the surface and bottom Ekman transports,

Brought to you by NOAA Central Library | Unauthenticated | Downloaded 01/16/24 05:03 PM UTC

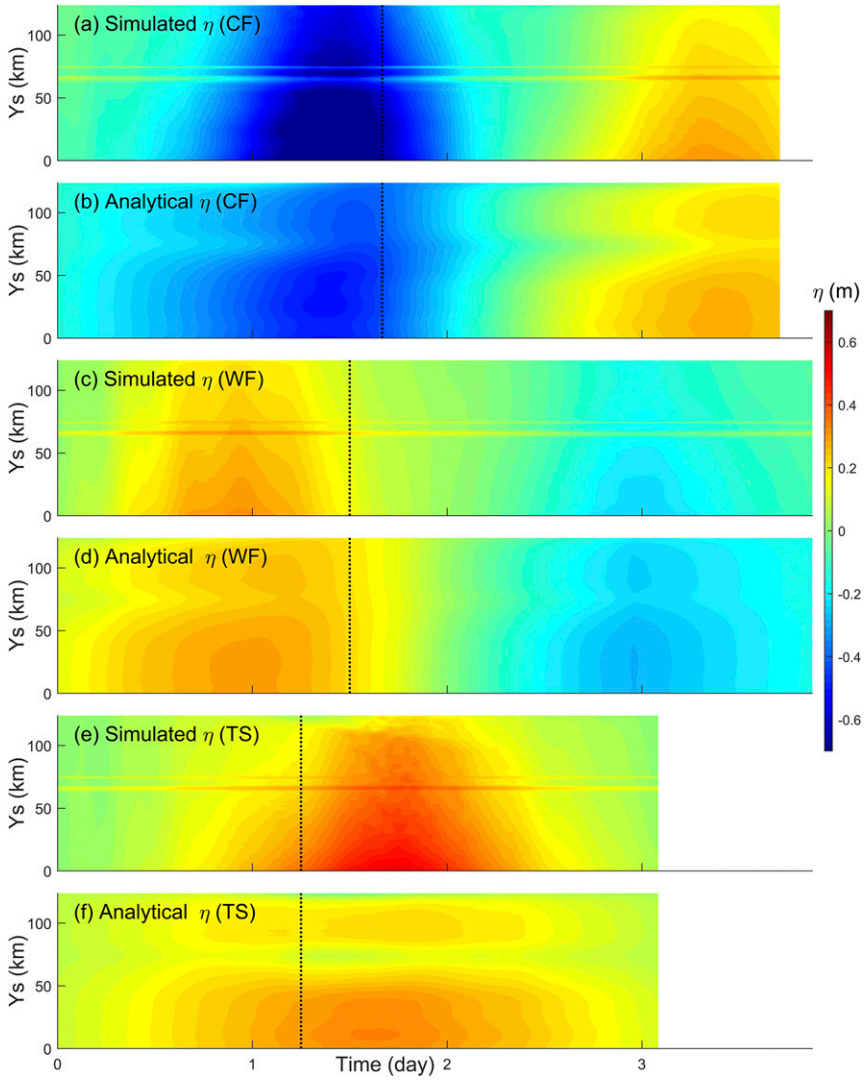

FIG. 12. Alongshore and temporal variability of (a),(c),(e) simulated and (b),(d),(f) analytical [Eq. (4.9)] sea level η along the 8-m isobath for the CF, WF, and TS events, respectively. The vertical line identifies the central point of each storm.

geostrophic transport due to alongshore shelf slope and transport associated with horizontal advection are found to be important cross-shore transport contributors. The alongshore variability in coastline orientation induces variations of the local along-/cross-shore wind component. Variation of the associated coastal sea level is the combined effect of the regional alongshore wind component and local along- and cross-shore wind components. The cross-shore length scales on which each wind component acts are around 80, 17, and 27 km, respectively.

In this work, variations of the wind velocity, storm duration, and the initial stratification are not considered. Impacts of tides and the Gulf Stream are also ignored. Further work is necessary to reliably assess the effects of these processes.

Acknowledgments. The two anonymous reviewers of this manuscript are thanked for their critical and insightful reviews that helped improve this manuscript significantly. The work presented was partially supported by the Southeast Coastal Observing Regional Association (SECOORA) pursuant to National Oceanic and Atmospheric Administration Award NA16NOS0120028 and the National Science Foundation (OCE 1603957). N. Kumar was supported by ONR N00014-17-1-2890. The manuscript preparation and finalization took place while G. Voulgaris was serving

Brought to you by NOAA Central Library | Unauthenticated | Downloaded 01/16/24 05:03 PM UTC

at NSF. Any opinions, findings, and conclusions or recommendations expressed in here are those of the authors and do not necessarily reflect the views of any of the funding organizations.

REFERENCES

Arthur, R. S., 1965: On the calculation of vertical motion in eastern boundary currents from determinations of horizontal motion. *J. Geophys. Res.*, **70**, 2799–2803, https://doi.org/10.1029/JZ070i012p02799.

Austin, J. A., and S. J. Lentz, 1999: The relationship between synoptic weather systems and meteorological forcing on the North Carolina inner shelf. *J. Geophys. Res.*, **104**, 18 159–18 185, https://doi.org/10.1029/1999JC900016.

——, and ——, 2002: The inner shelf response to wind-driven upwelling and downwelling. *J. Phys. Oceanogr.*, **32**, 2171–2193, https://doi.org/10.1175/1520-0485(2002)032<2171:TISRTW>2.0.CO;2.

Blanton, B. O., A. Aretxabaleta, F. E. Werner, and H. E. Seim, 2003: Monthly climatology of the continental shelf waters of the South Atlantic Bight. *J. Geophys. Res.*, **108**, 3264, https://doi.org/10.1029/2002JC001609.

——, and Coauthors, 2004: Barotropic tides in the South Atlantic Bight. *J. Geophys. Res.*, **109**, C12024, https://doi.org/10.1029/2004JC002455.

Blanton, J. O., L. P. Atkinson, L. J. Pietrafesa, and T. N. Lee, 1981: The intrusion of Gulf Stream water across the continental shelf due to topographically-induced upwelling. *Deep-Sea Res. I*, **28**, 393–405, https://doi.org/10.1016/0198-0149(81)90006-6.

Bradbury, J. A., B. D. Keim, and C. P. Wake, 2003: The influence of regional storm tracking and teleconnections on winter precipitation in the northeastern United States. *Ann. Assoc. Amer. Geogr.*, **93**, 544–556, https://doi.org/10.1111/1467-8306.9303002.

Brink, K. H., 2016: Cross-shelf exchange. *Annu. Rev. Mar. Sci.*, **8**, 59–78, https://doi.org/10.1146/annurev-marine-010814-015717.

Castelao, R., 2011: Intrusions of Gulf Stream waters onto the South Atlantic Bight shelf. *J. Geophys. Res.*, **116**, C10011, https://doi.org/10.1029/2011JC007178.

——, R. Chant, S. Glenn, and O. Schofield, 2010: The effects of tides and oscillatory winds on the subtidal inner-shelf cross-shelf circulation. *J. Phys. Oceanogr.*, **40**, 775–788, https://doi.org/10.1175/2009JPO4273.1.

Crépon, M., C. Richez, and M. Chartier, 1984: Effects of coastline geometry on upwellings. *J. Phys. Oceanogr.*, **14**, 1365–1382, https://doi.org/10.1175/1520-0485(1984)014<1365:EOCGOU>2.0.CO;2.

Davis, R. E., and R. Dolan, 1993: Nor'easters. *Amer. Sci.*, **81**, 428–439.

Dirks, R. A., J. P. Kuettner, and J. A. Moore, 1988: Genesis of Atlantic lows experiment (GALE): An overview. *Bull. Amer. Meteor. Soc.*, **69**, 148–160, https://doi.org/10.1175/1520-0477(1988)069<0148:GOALEA>2.0.CO;2.

Fan, Y., W. S. Brown, and Z. Yu, 2005: Model simulations of the Gulf of Maine response to storm forcing. *J. Geophys. Res.*, **110**, C04010, https://doi.org/10.1029/2004JC002479.

Fewings, M., S. J. Lentz, and J. Fredericks, 2008: Observations of cross-shelf flow driven by cross-shelf winds on the inner continental shelf. *J. Phys. Oceanogr.*, **38**, 2358–2378, https://doi.org/10.1175/2008JPO3990.1.

Gan, J., and J. S. Allen, 2002: A modeling study of shelf circulation off northern California in the region of the Coastal Ocean Dynamics Experiment: Response to relaxation of upwelling winds. *J. Geophys. Res.*, **107**, 3123, https://doi.org/10.1029/2000JC000768.

Gutierrez, B. T., G. Voulgaris, and P. A. Work, 2006: Cross-shore variation of wind-driven flows on the inner shelf in Long Bay, South Carolina, United States. *J. Geophys. Res.*, **111**, C03015, https://doi.org/10.1029/2005JC003121.

Horwitz, R., and S. J. Lentz, 2014: Inner-shelf response to cross-shelf wind stress: The importance of the cross-shelf density gradient in an idealized numerical model and field observations. *J. Phys. Oceanogr.*, **44**, 86–103, https://doi.org/10.1175/JPO-D-13-075.1.

——, and ——, 2016: The effect of wind direction on cross-shelf transport on an initially stratified inner shelf. *J. Mar. Res.*, **74**, 201–227, https://doi.org/10.1357/002224016820870648.

Keim, B. D., R. A. Muller, and G. W. Stone, 2004: Spatial and temporal variability of coastal storms in the North Atlantic Basin. *Mar. Geol.*, **210**, 7–15, https://doi.org/10.1016/j.margeo.2003.12.006.

Kumar, N., G. Voulgaris, J. C. Warner, and M. Olabarrieta, 2012: Implementation of the vortex force formalism in the coupled ocean-atmosphere-wave-sediment transport (COAWST) modeling system for inner shelf and surf zone applications. *Ocean Modell.*, **47**, 65–95, https://doi.org/10.1016/j.ocemod.2012.01.003.

——, ——, J. H. List, and J. C. Warner, 2013: Alongshore momentum balance analysis on a cuspate foreland. *J. Geophys. Res. Oceans*, **118**, 5280–5295, https://doi.org/10.1002/jgrc.20358.

Large, W. G., and S. Pond, 1981: Open ocean momentum flux measurements in moderate to strong winds. *J. Phys. Oceanogr.*, **11**, 324–336, https://doi.org/10.1175/1520-0485(1981)011<0324:OOMFMI>2.0.CO;2.

Lee, T. N., E. Williams, J. Wang, R. Evans, and L. Atkinson, 1989: Response of South Carolina continental shelf waters to wind and Gulf Stream forcing during winter of 1986. *J. Geophys. Res.*, **94**, 10 715–10 754, https://doi.org/10.1029/JC094iC08p10715.

Lentz, S. J., 2001: The influence of stratification on the wind-driven cross-shelf circulation over the North Carolina shelf. *J. Phys. Oceanogr.*, **31**, 2749–2760, https://doi.org/10.1175/1520-0485(2001)031<2749:TIOSOT>2.0.CO;2.

——, 2008: Observations and a model of the mean circulation over the Middle Atlantic Bight continental shelf. *J. Phys. Oceanogr.*, **38**, 1203–1221, https://doi.org/10.1175/2007JPO3768.1.

——, and M. R. Fewings, 2012: The wind- and wave-driven inner-shelf circulation. *Annu. Rev. Mar. Sci.*, **4**, 317–343, https://doi.org/10.1146/annurev-marine-120709-142745.

——, R. T. Guza, S. Elgar, F. Feddersen, and T. H. C. Herbers, 1999: Momentum balances on the North Carolina inner shelf. *J. Geophys. Res.*, **104**, 18 205–18 226, https://doi.org/10.1029/1999JC900101.

Marchesiello, P., J. C. McWilliams, and A. Shchepetkin, 2001: Open boundary conditions for long-term integration of regional oceanic models. *Ocean Modell.*, **3**, 1–20, https://doi.org/10.1016/S1463-5003(00)00013-5.

Mather, J. R., H. Adams III, and G. A. Yoshioka, 1964: Coastal storms of the eastern United States. *J. Appl. Meteor.*, **3**, 693–706, https://doi.org/10.1175/1520-0450(1964)003<0693:CSOTEU>2.0.CO;2.

Mitchum, G. T., and A. J. Clarke, 1986: The frictional nearshore response to forcing by synoptic scale winds. *J. Phys. Oceanogr.*, **16**, 934–946, https://doi.org/10.1175/1520-0485(1986)016<0934:TFNRTF>2.0.CO;2.

Brought to you by NOAA Central Library | Unauthenticated | Downloaded 01/16/24 05:03 PM UTC

Mukai, A. Y., J. J. Westerink, and R. A. Luettich, 2002: Guidelines for using Eastcoast 2001 database of tidal constituents within western North Atlantic Ocean, Gulf of Mexico and Caribbean Sea. U.S. Army Corps of Engineers Tech. Note ERDC/CHL CHETN-IV-40, 20 pp., http://www.unc.edu/ims/adcirc/publications/2002/2002_Mukai02.pdf.

Muller, R. A., and G. W. Stone, 2001: A climatology of tropical storm and hurricane strikes to enhance vulnerability prediction for the southeast US coast. *J. Coastal Res.*, **17**, 949–956.

Pringle, J. M., 2002: Enhancement of wind-driven upwelling and downwelling by alongshore bathymetric variability. *J. Phys. Oceanogr.*, **32**, 3101–3112, https://doi.org/10.1175/1520-0485(2002)032<3101:EOWDUA>2.0.CO;2.

Raymond, W. H., and H. L. Kuo, 1984: A radiation boundary condition for multi-dimensional flows. *Quart. J. Roy. Meteor. Soc.*, **110**, 535–551, https://doi.org/10.1002/qj.49711046414.

Shchepetkin, A. F., and J. C. McWilliams, 2005: The Regional Oceanic Modeling System (ROMS): A split-explicit, free-surface, topography-following-coordinate oceanic model. *Ocean Modell.*, **9**, 347–404, https://doi.org/10.1016/j.ocemod.2004.08.002.

Smith, P. C., and J. I. MacPherson, 1987: Cross-shore variations of near-surface wind velocity and atmospheric turbulence at the land-sea boundary during CASP. *Atmos.–Ocean*, **25**, 279–303, https://doi.org/10.1080/07055900.1987.9649276.

Suanda, S. H., F. Feddersen, and N. Kumar, 2017: The effect of barotropic and baroclinic tides on coastal stratification and mixing. *J. Geophys. Res. Oceans*, **122**, 10 156–10 173, https://doi.org/10.1002/2017JC013379.

Tilburg, C. E., 2003: Across-shelf transport on a continental shelf: Do across-shelf winds matter? *J. Phys. Oceanogr.*, **33**, 2675–2688, https://doi.org/10.1175/1520-0485(2003)033<2675:ATOACS>2.0.CO;2.

Umlauf, L., and H. Burchard, 2003: A generic length-scale equation for geophysical turbulence models. *J. Mar. Res.*, **61**, 235–265, https://doi.org/10.1357/002224003322005087.

Walter, R. K., E. C. Reid, K. A. Davis, K. J. Armenta, K. Merhoff, and N. J. Nidzieko, 2017: Local diurnal wind-driven variability and upwelling in a small coastal embayment. *J. Geophys. Res. Oceans*, **122**, 955–972, https://doi.org/10.1002/2016JC012466.

Warner, J. C., B. Armstrong, R. He, and J. B. Zambon, 2010: Development of a coupled ocean–atmosphere–wave–sediment transport (COAWST) modeling system. *Ocean Modell.*, **35**, 230–244, https://doi.org/10.1016/j.ocemod.2010.07.010.

Weber, J. E., 1983: Steady wind-and wave-induced currents in the open ocean. *J. Phys. Oceanogr.*, **13**, 524–530, https://doi.org/10.1175/1520-0485(1983)013<0524:SWAWIC>2.0.CO;2.

Whitney, M. M., and J. S. Allen, 2009: Coastal wind-driven circulation in the vicinity of a bank. Part I: Modeling flow over idealized symmetric banks. *J. Phys. Oceanogr.*, **39**, 1273–1297, https://doi.org/10.1175/2008JPO3966.1.

Wu, X., G. Voulgaris, and N. Kumar, 2017: Climatology and parameterization of synoptic weather systems for long term coastal ocean modeling applications: A case study from the South Carolina coast. *Ocean Dyn.*, **67**, 1231–1249, https://doi.org/10.1007/s10236-017-1084-x.

Zhang, X., S. F. DiMarco, D. C. Smith IV, M. K. Howard, A. E. Jochens, and R. D. Hetland, 2009: Near-resonant ocean response to sea breeze on a stratified continental shelf. *J. Phys. Oceanogr.*, **39**, 2137–2155, https://doi.org/10.1175/2009JPO4054.1.

Brought to you by NOAA Central Library | Unauthenticated | Downloaded 01/16/24 05:03 PM UTC